Electrochimica Acta 570 (2026) 148936

Contents lists available at ScienceDirect

Electrochimica Acta

journal homepage: www.journals.elsevier.com/electrochimica-acta

Interplay between corrosion behaviour and bioactivity of TiO_2 nanotubes on Ti6Al4V in physiological and inflammatory environments

M.L. Lazzara [a], F. Di Franco [a], D. Pupillo [b], M. Santamaria [a,*]

[a] *Dipartimento di Ingegneria, Università degli Studi di Palermo, 90128 Palermo, Italy*
[b] *Istituto di tecnologie avanzate per l'energia "Nicola Giordano", Consiglio Nazionale delle Ricerche (CNR-ITAE), 90126 Messina, Italy*

ARTICLE INFO

Keywords:
TiO_2 Nanotubes
Ti6Al4V
Corrosion
Bioactivity
Inflammation
Hydroxyapatite growth
Biomedical implants

ABSTRACT

Titanium and its alloys are widely used for biomedical applications in orthopedics and dentistry; however, achieving optimal osseointegration while maintaining corrosion resistance under inflammatory conditions remains challenging. In this study, TiO_2 nanotubes (NTs) were fabricated on Ti6Al4V alloy by electrochemical anodization and characterized to assess corrosion behaviour and bioactivity in both physiological and inflammatory simulated environments. Photoelectrochemical analysis revealed that the NTs-modified samples exhibit localized electronic states within the mobility gap, enhancing electronic conduction through the nanostructured oxide. Long-term immersion tests, combined with electrochemical impedance spectroscopy and ICP-OES measurements, demonstrated that NT-modified surfaces exhibit superior corrosion resistance compared to bare Ti6Al4V alloy, with cumulative ion release approximately half an one order of magnitude lower after 168 h of immersion . SEM analysis confirmed the morphological stability of NTs after 168 h of immersion in inflammatory media, whereas bare samples showed preferential dissolution of the β-phase. Despite an increase in corrosion current density and a reduction of the passive region under inflammatory conditions, the nanotubular oxide facilitated Ca/P accumulation and hydroxyapatite formation in physiological environment. These results highlight that controlling the top-layer morphology through anodic TiO_2 nanotubes enables an effective balance between corrosion resistance and biological performance in implant-relevant environments.

1. Introduction

Metallic materials are widely investigated for use in implantable medical devices designed to replace or support damaged tissues. Load-bearing implants must exhibit excellent corrosion resistance, adequate mechanical strength, biocompatibility, and strong osseointegration to ensure long-term clinical success and minimize the risk of failure or revision surgery [1–4]. However, surgical implantation inevitably causes local tissue injury, triggering an acute inflammatory response lasting approximately one week. This early phase is crucial for wound healing and integration, as new tissue and blood vessels form around the implant [5].

Among metallic biomaterials, titanium and its alloys have gained attention due to their favourable strength-to-weight ratio, elastic modulus close to that of bone, and excellent corrosion resistance in physiological environments [1,6]. Ti6Al4V, an $\alpha+\beta$ alloy combining the corrosion resistance of the hexagonal close-packed (α) phase with the strength and heat treatability of the body-centered cubic (β) phase, is the most extensively used titanium alloy in orthopedics for joint replacements and fixation devices [7,8]. Nevertheless, titanium and its alloys are inherently bioinert, resulting in limited bone–implant bonding and delayed osseointegration [9]. Additionally, the possible release of vanadium and aluminium ions from Ti6Al4V substrate may induce inflammatory or cytotoxic effects, compromising long-term implant performance [10]. Extending implant durability and improving bone integration therefore remain key objectives in orthopedic device development.

To overcome these limitations, surface modification techniques have been explored to enhance the bioactivity and electrochemical stability of Ti-based implants [2,11]. Among them, anodization is a versatile and cost-effective method capable of producing TiO_2 nanostructures, such as ordered nanotube arrays, with tunable morphology [12]. TiO_2 nanotubes (NTs) enhance cell adhesion, proliferation, and osteogenic differentiation, while also reducing bacterial colonization [13]. Moreover, they serve as effective scaffolds for hydroxyapatite nucleation, promoting osteoconductivity and transforming the bioinert titanium

---

* Corresponding author.
E-mail address: monica.santamaria@unipa.it (M. Santamaria).

https://doi.org/10.1016/j.electacta.2026.148936
Received 9 February 2026; Received in revised form 11 April 2026; Accepted 21 April 2026

surface into a bioactive one.

Hydroxyapatite (HA, $Ca_{10}(OH)_2(PO_4)_6$)) is a calcium orthophosphate, a salt of the tribasic orthophosphoric acid H_3PO_4, that at physiological pH represents the most stable form of calcium phosphate [14,15]. HA plays a key role in osteoinduction, the process by which stem cells differentiate into osteoblasts, leading to bone regeneration [16,17]. Its presence on Ti surfaces improves biocompatibility and osseointegration. Since HA formation is favoured by local alkalinization, the electrochemical behaviour and solid-state properties of the titanium oxide film critically influence the material's bioactivity and ability to support its growth.

Despite their promising biological properties, TiO_2 nanotubes on Ti6Al4V have been only partially characterized in terms of electrochemical and corrosion behaviour [18]. A clear consensus on their response under physiological and inflammatory conditions is still lacking, due to the limited number of studies and the use of different simulated solutions [19–24]. In particular, the incorporation of alloying elements (Al, V) into the anodic oxide and its influence on electronic and corrosion properties are not fully elucidated. Inflammatory media, rich in reactive oxygen species (ROS) and acidic metabolites, can destabilize oxide films and accelerate degradation, posing additional challenges to implant longevity [25,26]. Recent research emphasizes the role of semiconductor properties in anodic oxides grown on Ti6Al4V for controlling corrosion [27,28]. However, the link between the electronic features of TiO_2 NTs on Ti6Al4V and their electrochemical behaviour remains underexplored.

To address this gap, the present study investigates the formation, morphology, and electrochemical performance of anodically grown TiO_2 nanotubes on Ti6Al4V. The electronic properties of the oxide layers are correlated with their corrosion behaviour in Hank's Balanced Salt Solution (HBSS) and Severe Inflammatory Condition Solution (SICS), two simulated physiological environments representing normal and inflamed tissue conditions. Additional immersion tests evaluate ions release and hydroxyapatite precipitation, aiming to enhance osteoconductivity and overall bioactivity. Ultimately, this work seeks to establish a relationship between the electronic structure of TiO_2 NTs on Ti6Al4V and its electrochemical behaviour, contributing to the design of more durable, biocompatible, and clinically reliable implant surfaces.

2. Materials and methods

2.1. Sample preparations

Titanium alloy (Ti6Al4V) foils (Grade 5, ASTM B265) with a thickness of 0.6 mm were used as the metallic substrate for the production of TiO_2 nanotubes via a one-step anodization process. Supplied by Goodfellow Cambridge Ltd. (United Kingdom), the sheets had a chemical composition of 90% titanium, 6% aluminium, and 4% vanadium. They were degreased by ultrasonic cleaning in acetone for 5 min, rinsed with deionized water, and air-dried. Chemical etching was performed in a mixture of hydrofluoric acid (39.5%), nitric acid (69.0%), and deionized water (1:4:5 v/v) for 40 s under ultrasonic agitation, followed by a 10-minute ultrasonic rinse in deionized water. After drying in air, the samples were immediately ready for further use.

For comparative SEM observations, selected samples were mechanically polished using silicon carbide (SiC) abrasive papers with grit sizes ranging from P320 to P1200 in order to compare their surface morphology with that of chemically etched specimens.

2.2. Titania nanotubes array growth by anodization

Titania nanotubes (NTs) layer was grown on Ti6Al4V substrates using an electrolyte containing 0.50 wt.% of ammonium fluoride (NH_4F, Carlo Erba Reagents), ethylene glycol (EG, Carlo Erba Reagents), and 50 wt.% of deionized water. Anodic oxidation was carried out potenziostatically at 30 V for 60 min using a two-electrode cell configuration setup, with the Ti6Al4V samples acting as the anode and an 99.9% pure aluminium foil served as the cathode. Soon after the anodization process, the samples were cleaned by ultrasonication, first in ethanol for 5 min, then in deionized water for 10 min. In the final step, a thermal treatment was performed: the samples were annealed in air at 450 °C for 60 min and allowed to cool inside the furnace.

2.3. Surface morphology and structural characterization

The morphology of the samples was investigated using a FEI Quanta 200 FEG SEM microscope, equipped with an Energy-Dispersive X-ray Spectrum (EDAX Genesis XM 4) system. Micrographs were obtained at 30 kV with the SEM operating in High Vacuum mode. EDX analysis was conducted by slowing down the voltage to 15 kV, and the EDX spectra were fitted using the EDX Genesis software. SEM images were utilized for the quantitative analysis of nanotube diameter, length and inter-tube spacing. Image analysis was performed using the open-source software ImageJ on multiple SEM images. A total of $n = 100$ individual nanotubes were measured to ensure statistical significance. The results are reported as mean ± standard deviation. Raman spectroscopy was carried out using a Renishaw inVia Raman Microscope equipped with a 50 × microprobe and a CCD detector with a Nd:YAG laser operating at 532 nm.

2.4. Photoelectrochemical characterization

The experimental setup for the photoelectrochemical measurements includes a 1000 W UV–VIS xenon lamp connected to a monochromator (Kratos), enabling monochromatic irradiation of the sample surface through the quartz windows of the photoelectrochemical cell. The specimens were characterized in a 0.1 M ammonium biborate tetrahydrate (ABE, $(NH_4)_2B_4O_7 \cdot 4\ H_2O$, pH ~8.5) aqueous solution. The photocurrent measurements were carried out by applying a potentiostatic control, regulated by a versaSTAT3 potentiostat (AMETEK), for the different samples, which served as the working electrodes. A Pt wire was used as the counter electrode and an Ag/AgCl electrode (0.197 V vs. SHE) served as the reference electrode for all photoelectrochemical experiments. The resulting current was analyzed using the lock-in amplifier (EG&G), which was coupled with a mechanical chopper operating at a frequency of 13 Hz to isolate the photocurrent from the total current circulating in the cell. The photocurrent spectra (i.e., photocurrent vs wavelength) were corrected for the relative photon flux of the light source at each wavelength, and the photocurrent yield in arbitrary current units is presented on the y-axis, reflecting the efficiency of the lamp-monochromator system.

The stationary photocurrent values for a few selected wavelengths and at different applied potentials were recorded by manually chopping irradiation, in order to get information from the photocurrent transients about the semiconductor behaviour and from the dependence of the photocurrent as a function of potential under constant wavelength to estimate the flat band potential (i.e. photocaracteristics).

All experiments were conducted at room temperature (25 °C ± 2 °C) and in air.

2.5. Electrochemical measurements

Electrochemical measurements were performed using a Gamry Interface 1010E potentiostat in two Simulated Body Fluids (see composition in Table 1) at 37 °C : Hanks' Balanced Salt Solution (HBSS) and a modified HBSS simulating severe inflammatory conditions (SICS). In SICS, lactic acid (LA, 85% wt., Sigma-Aldrich) and hydrogen peroxide (H_2O_2, 35% wt., Carlo Erba Reagents) were added at a concentration of 150 mM. Although higher than typical physiological levels [25,29], such supra-physiological concentrations are commonly adopted in the literature to accelerate degradation processes and simulate extreme oxidative stress conditions at the implant interface [30,31]. The final pH was

Table 1
Composition of simulating solutions employed: Hank's Balanced Salt Solution (HBSS, pH=7.4) and Severe Inflammatory Conditions Solution (SICS, pH=2).

Substance	HBSS	SICS
NaCl	8.00 g L^{-1}	8.00 g L^{-1}
KCl	0.40 g L^{-1}	0.40 g L^{-1}
$NaHCO_3$	0.35 g L^{-1}	0.35 g L^{-1}
$NaH_2PO_4 \cdot H_2O$	0.25 g L^{-1}	0.25 g L^{-1}
$Na_2HPO_4 \cdot H_2O$	0.06 g L^{-1}	0.06 g L^{-1}
$CaCl_2 \cdot 2H_2O$	0.19 g L^{-1}	0.19 g L^{-1}
$MgCl_2$	0.19 g L^{-1}	0.19 g L^{-1}
$MgSO_4 \cdot 7H_2O$	0.06 g L^{-1}	0.06 g L^{-1}
Glucose	1.00 g L^{-1}	1.00 g L^{-1}
Lactic acid	-	150 mM
H_2O_2	-	150 mM

7.4 for HBSS and 2 for SICS, respectively, and the cell volume was 100 mL. While this acidic value is not representative of bulk physiological conditions, pH values as low as 2–3 have been reported locally in the vicinity of implants under severe inflammatory conditions [32].

A three-electrode setup was employed with Ti6Al4V samples (bare and anodized) as the working electrode, a platinum mesh as counter electrode, and Ag/AgCl (0.197 V vs. SHE) as reference. The open circuit potential (E_{OCP}) was monitored for 30 min, until a steady-state value was reached. Electrochemical impedance spectroscopy (EIS) spectra were collected at E_{OCP} by applying a sinusoidal signal with an amplitude of 10 mV over a frequency range of 10 mHz to 100 kHz. Polarization curves were recorded immediately afterward, starting from −150 mV vs. E_{OCP} and scanning anodically at 2 mV·s^{-1}. Analysis of the EIS results was performed with ZSimpWin software. All electrochemical measurements were performed in triplicate to ensure reproducibility.

In all the experiments, the current and the impedance were normalized by the geometric surface of the samples.

2.6. *Hydroxyapatite precipitation*

To assess the biological activity of anodized Ti6Al4V samples, hydroxyapatite (HA) formation on the nanotubular oxide layers was evaluated by immersing the samples in Hanks' Balanced Salt Solution (HBSS) (composition in Table 1). The samples were placed in a 1-liter open-top bottle containing 700 mL of HBSS and incubated at 37 °C for 28 days, with the solution refreshed every 72 h. After the immersion period, the samples were removed, rinsed with deionized water, and air-dried. The presence of HA precipitation was analyzed using Scanning Electron Microscopy (SEM) coupled with EDX and Raman spectroscopy. The immersion test was performed in triplicate to ensure reproducibility of the results.

2.7. *Immersion tests and ions release evaluation*

To assess the long-term effects of surface treatments and the performance of the samples in the selected corrosive environments, immersion tests were carried out in either HBSS or SICS. The experiments lasted 7 days and were conducted in an incubator at a constant temperature of 37 °C. Samples were placed in sealed sterilized half-filled 50 mL centrifuge tubes to minimize evaporation and immersed in a defined volume of solution, ensuring a surface area-to-volume ratio of 20 mL/cm^2. At 24, 72, and 168 h, the specimens were taken out of the electrolyte and then transferred into fresh solution to continue the test under the same surface area-to-volume ratio conditions. The solutions collected at each interval were stored for subsequent cumulative ion-release analysis. The electrolytes were acidified with 2% v/v HNO_3, and the concentrations of Ti, Al, and V were quantified by Inductively Coupled Plasma-Optical Emission Spectroscopy (ICP-OES) using a Perkin Elmer OPTIMA 2100 DV instrument. All immersion tests were performed in triplicate to ensure reproducibility of the results.

3. Results and discussion

3.1. *Samples preparation*

SEM micrographs of bare Ti6Al4V samples prior to anodizing are shown in Fig. 1. The mechanically polished surface appears relatively smooth (Fig. 1a), while chemical etching in HF (39.5%)–HNO_3 (69.0%)–H_2O (1:4:5 v/v) for 40 s results in a roughened morphology. Etching enhances the visibility of the dual-phase microstructure, improving the contrast between α and β phases [33].

According to Sittig et al. [34], this effect is due to the preferential dissolution of the α-phase, leading to an enrichment of the β-phase at the surface when exposed to HF–HNO_3 mixtures. Specifically, the α-phase is preferentially attacked, particularly near regions of β-phase segregation. This is attributed to the redox potential difference between the two phases, with the α-phase being more anodic. In contrast, the β-phase, enriched in vanadium, is more resistant to fluoride-induced corrosion, forming protruding ridges [35,36], as seen in the inset of Fig. 1c.

Prolonged etching (90 s) caused excessive surface roughening, which could compromise subsequent anodization. Therefore, 40 s was selected as the optimal etching time, ensuring effective surface cleaning and clear microstructural contrast without inducing excessive damage.

High-magnification SEM of the 40 s etched sample is shown in Fig. 2. EDX analysis of regions A and B (Fig. 2 and Table 2) confirms compositional differences: the darker α-phase (region A) shows a lower V/Ti ratio and higher Al/Ti ratio, while the brighter β-phase (region B) exhibits a higher V/Ti ratio and lower Al/Ti ratio. These results confirm that the β-phase is enriched in vanadium and depleted in aluminium.

3.2. *Titania nanotubes oxide layers growth*

The current density–time transient recorded during anodization of Ti6Al4V (see Fig. 3a) exhibits the typical features commonly reported for titanium under similar conditions, namely an initial decay, followed by a slight increase, and finally a steady-state regime. This similarity suggests that the underlying growth mechanism is largely analogous to that established for Ti.

The initial decrease in current density can be attributed to the formation of a compact oxide layer under high-field conditions. During the early stage of the anodizing process metal ions produced at the metal/oxide interface migrate outward toward the oxide/electrolyte interface driven by the applied electric field with similar transport number. Indeed, according to the literature the transport number for Ti^{4+}, Al^{3+} and V^{5+} are 0.39, 0.40 and 0.28, respectively [37]. Moreover, O^{2-} ions produced by water dissociation and F^- ions present into the electrolyte migrate inward, the latter ion being faster than the former (see Fig. 3b).

As anodization proceeds, the presence of fluoride ions induces localized dissolution of the oxide, leading to the nucleation of nanoscale pores. This transition is reflected in the subsequent increase in current density, which is associated with the enlargement of the electrochemically active surface area. The dissolution phenomena involve all the alloy constituents. As reported in the literature [38], during the anodizing of titanium in a fluoride containing environment the following reactions can occur:

$$Ti^{4+} + 6F^{-} \rightarrow [TiF_6]^{2-} \tag{1}$$

$$TiO_2 + 6F^{-} + 4H^{+} \rightarrow [TiF_6]^{2-} + 2H_2O \tag{2}$$

Concerning aluminium, anodization in fluoride-containing electrolytes leads to the field-assisted ejection of Al^{3+} ions from the growing oxide film. According to the literature, this process is promoted by fluoride adsorption at the oxide surface, which replaces hydroxyl species and facilitates the formation of soluble aluminium–fluoride complexes, such as AlF^{2+} and AlF_2^{+} thereby contributing to the development of a porous anodic film [39]. Regarding vanadium, previous studies have

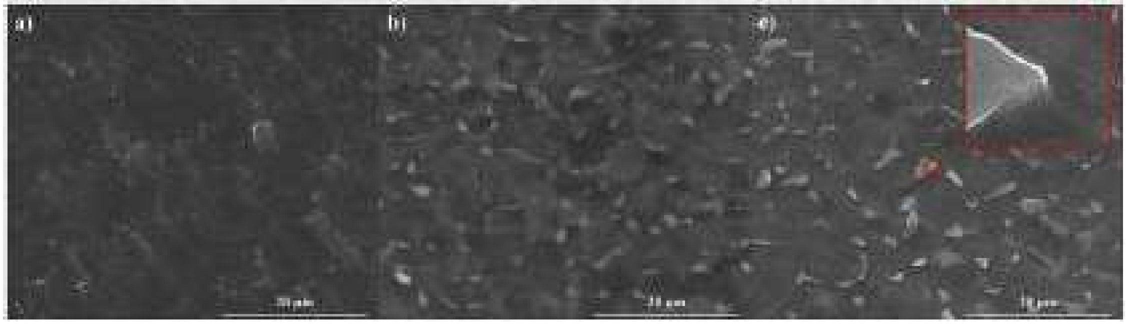

Fig. 1. SEM micrographs showing the surface morphology of Ti6Al4V samples: (a) mechanically polished substrate, (b) after 40 s and (c) after 90 s of chemical etching.

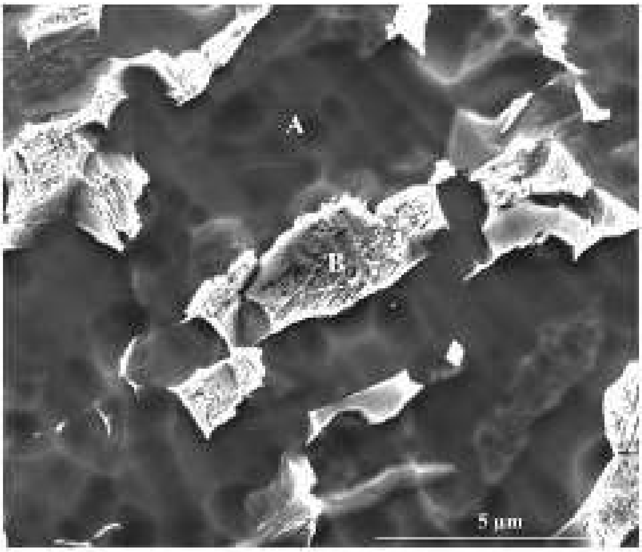

Fig. 2. High-magnification SEM image of the 40 s chemically etched Ti6Al4V surface, highlighting the α-phase (A) and β-phase (B).

Table 2
Quantitative EDX results (at.%) obtained from local analyses at regions A (α-phase) and B (β-phase), related to Fig. 2.

Sample	Local Area	Al/Ti	V/Ti
Bare Ti6Al4V	A	0.15	0.02
	B	0.11	0.11

shown that its anodization efficiency in aqueous solutions is very low even in the absence of fluoride ions (~10%, according to [40]), indicating a strong tendency toward dissolution or limited incorporation into the growing oxide.

The formation of such soluble species at the oxide/electrolyte interface reduces the overall oxide growth efficiency. At intermediate fluoride concentrations (0.05 wt% $<$ [F^-] $<$ 1 wt%), a competition between oxide formation and metal ion solvatization is established, which can lead to the development of porous or nanotubular morphologies (see Fig. 3c,d).

The onset of self-organization in anodic nanotube formation arises from a delicate balance between field-assisted oxide growth and fluoride-induced chemical dissolution. At intermediate fluoride concentrations, this competition leads to an instability in the initially formed compact oxide: localized dissolution sites develop, initiating nanoscale pores. This marks the transition from a compact to a self-organized structure, typically reflected in the current–time response by an initial decay (compact oxide formation), followed by a current increase due to pore nucleation, and finally a steady-state regime corresponding to the development of an ordered nanotubular or nanoporous layer. A key factor in sustaining self-organization is the formation of a fluoride-rich interfacial layer at the metal–oxide interface (see Fig. 3c), resulting from the high mobility of fluoride ions relative to oxygen species. This layer facilitates continuous dissolution at the pore bottom, maintaining a thin barrier oxide and a high local electric field, which is essential for ordered growth.

In Ti6Al4V alloys, the anodic response is strongly influenced by the microstructural distinction between α and β phases. The α-phase, which is Al-rich, tends to form a more stable oxide during anodization, with a higher degree of incorporation of aluminium species within the growing nanotube walls, contributing to structural stability. In contrast, the β-phase, which is enriched in vanadium, exhibits a higher tendency toward oxide dissolution and material removal under the same anodizing conditions. As a result, the anodized surface displays a non-uniform morphology, where β-phase regions appear more recessed compared to α-phase regions. This behaviour is consistent with enhanced local dissolution in V-rich areas, which can lead to partial breakdown of the passive oxide film.

SEM analysis was employed to investigate the impact of the microstructure and phase composition of Ti6Al4V on its surface morphology after anodization. SEM images at different magnifications of titania nanotubes (NTs) formed on Ti6Al4V are shown in Figs. 4a–f.

Highly uniform nanotube layers form predominantly over the α-phase, while the β-phase exhibits a not well-defined nanostructure (see Fig. 4a–c). The anodic oxide is not entirely continuous; localized cracks and inhomogeneities indicate uneven growth due to the differing electrochemical properties of the two phases. The presence of both α and β phases in the Ti6Al4V alloy results in markedly different nanotube formation behaviours, leading to the formation of a heterogeneous oxide morphology under the investigated conditions. EDX analysis (reported in Table 3) reveals the presence of Al and V incorporated into the NT-modified Ti6Al4V samples during the anodization process.

The micrographs reveal a well-ordered array of vertically aligned nanotubes with an internal diameter of 97.7 ± 14.4 nm and an intertube distance of 22.7 ± 7.2 nm (mean ± standard deviation). The cross-sectional view (see Fig. 4f) shows that the nanotubes have an average length of approximately 978.8 ± 54.1 nm. Additionally, a histogram of the nanotube diameter distribution, along with the corresponding Gaussian fit, has been included in the Supporting Information (see Fig. S1), providing a more comprehensive quantitative description of the nanotube morphology.

A subsequent thermal treatment at 450 °C for 60 min was applied to remove residual fluorides, enhancing the chemical stability of the nanotubes. This process is known to promote the crystallization of TiO_2 nanotubes into the anatase phase, thereby stabilizing the nanostructure while eliminating fluoride ions that could induce cytotoxic effects in biological environments. In addition, annealing improves surface wettability and favors hydroxyapatite deposition, likely as a

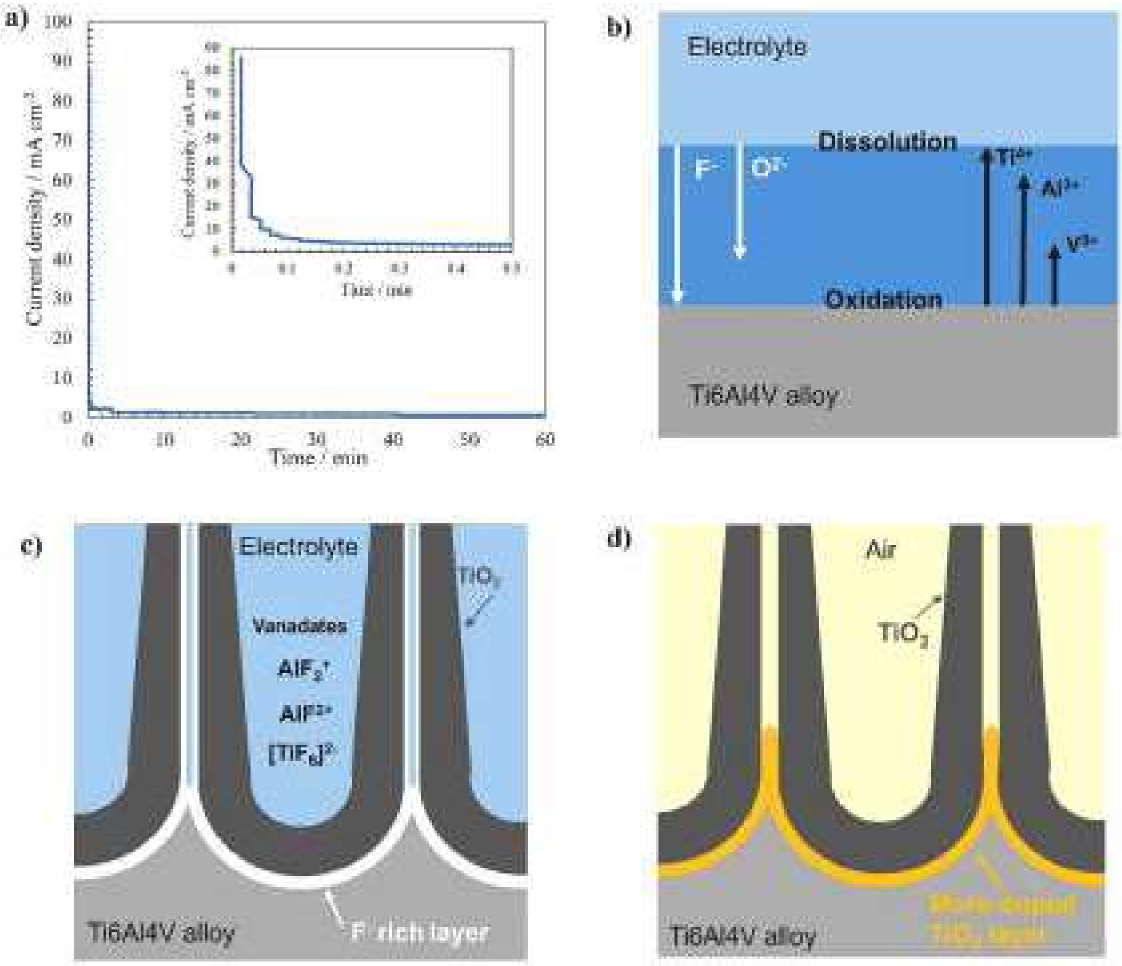

Fig. 3. a) Current density–time curve during the growth of TiO_2 nanotube (NT) layers on Ti6Al4V by potentiostatic anodization at 30 V for 60 min in an electrolyte containing 0.5 wt.% NH_4F, ethylene glycol, and 50 wt.% deionized water; b) Schematic illustration of field-assisted ion transport through the oxide layer in the presence of fluoride ions; c) Schematic cross-sectional view of the Ti6Al4V surface showing the formation of soluble complexes from alloy constituents during anodization; d) Schematic cross-sectional view of the Ti6Al4V surface after thermal treatment at 450 °C for 60 min.

consequence of anatase phase formation [41]. The formation of anatase TiO_2 after annealing was confirmed by Raman spectroscopy (Supporting Information, Fig. S2), showing characteristic bands at 144, 196, 398, 513, and 638 cm^{-1}, slightly shifted with respect to stoichiometric anatase, indicating the presence of a defective TiO_2 nanostructure [42]. In addition, the ~100 nm diameter nanotubes formed by anodic oxidation induce a capillary effect, enhancing hydrophilicity and promoting bone cell attachment [43].

The proposed NTs growth mechanisms and the observed NTs morphology are consistent with previous studies [12,44,45]. These works show that, due to different oxide growth kinetics, NTs formation varies between phases: the α-phase typically develops well-defined NTs, whereas the β-phase forms disordered oxides [19,44–46].

Such differences arise from variations in composition (Al-rich α, V-rich β) and crystal structure (HCP vs. BCC). The higher Ti diffusivity in the β-phase promotes rapid formation of a compact oxide layer, while the α-phase tends to repassivate due to its higher Al content [12]. As discussed above, vanadium increases oxide solubility, leading to earlier pore formation in the β-phase. Once pores are established, the growth behaviour reverses, with the α-phase supporting faster and more uniform NTs growth, resulting in longer NTs with thinner walls [47,48].

3.3. Photoelectrochemical characterization

A photoelectrochemical characterization was performed to investigate the electronic properties of thermally treated Ti6Al4V nanotube arrays (NTs). Fig. 5a shows the photocurrent response as a function of the wavelength under monochromatic illumination, measured in 0.1 M ABE under constant bias conditions at 1 V vs Ag/AgCl. The use of a non-aggressive aqueous solution ensured the stability of the investigated oxide layer. To extend the investigation to lower photon energies, spectra above 400 nm were acquired using a UV cut-off filter (orange curve).

Assuming indirect optical transitions for the nanostructured oxide, the optical band gap energy (E_g) was estimated using the relation [49]:

$$(Q_{ph}\,h\nu)^n \propto (h\nu - E_g) \tag{3}$$

where hν is the photon energy and $n = 0.5$ for indirect transitions. In the spectral region near the band gap, the photocurrent yield (Q_{ph}) is proportional to the material's absorption characteristics, allowing E_g to be determined from the extrapolation of $(Q_{ph}\ h\nu)^{0.5}$ vs hν (see inset of Fig. 5a).

The NTs layer exhibits a pronounced photocurrent tail in the low-energy region with optical transitions up to ~ 1.2 eV, suggesting strong electronic modification induced by the alloy substrate. Indeed, band gap reported for anatase is 3.20 eV, while a lower value (3.05 eV) is reported for rutile [28,50]. The presence of this photocurrent tail can be explained by the formation of localized states inside the mobility gap of titanium oxides, that are created by Al and V incorporated during the anodization process as well as during the high temperature annealing.

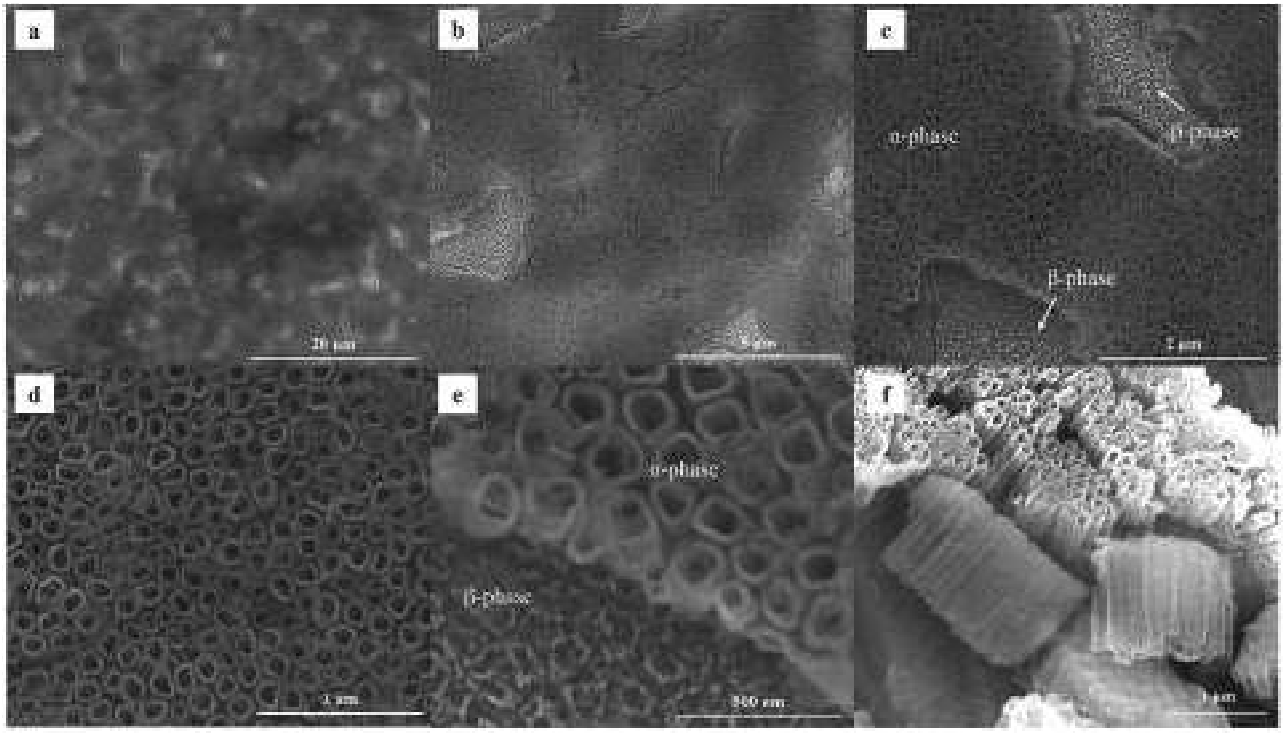

Fig. 4. SEM micrographs of TiO_2 nanotube (NT) arrays grown on Ti6Al4V by anodization in 0.5 wt.% NH_4F, ethylene glycol, and 50 wt.% deionized water at 30 V for 60 min: (a) low-magnification (5000 ×) overview of the NTs layer morphology; (b) intermediate magnification (20,000 ×) showing NTs distribution across α and β phases; (c) detailed morphology on both phases at 50,000 ×; (d) high-resolution (100,000 ×) detail of NTs on the α phase and (e) at the α/β interface (200,000 ×); (f) cross-sectional view (60,000 ×) illustrating nanotube length and vertical alignment.

Table 3
Results from EDX analysis (at.%) for nanotube arrays grown of Ti6Al4V, related to Fig. 4d.

Element	Wt %	At %
Ti	65.01	40.62
O	28.44	53.19
Al	4.50	4.99
V	2.05	1.20

They strongly affect the electronic properties of the anodic layers since they play the role of dopants.

Photocurrent vs potential curves (photocharacteristics) were obtained in 0.1 M ABE by irradiating the nanostructured oxide films at different wavelengths (260, 290, 320, 350, 400, 500, 600, and 650 nm), as reported in Fig. 5b-c. When the applied bias was shifted toward more cathodic potentials, the photocurrent did not decrease monotonously. Furthermore, dark–light current transients recorded at $\lambda = 320$ nm, at applied potentials of 1 V vs. Ag/AgCl and −0.2 V vs. Ag/AgCl (Fig. 5d), confirmed that the stationary photocurrent is anodic.

Notably, the same non monotonic trend showed in the photocharacteristics was observed in the differential capacitance recorded at different frequencies, displayed in Fig. 5e. As reported for TiO_2 NTs grown by anodization on commercially pure titanium in the same conditions [51], the measured capacitance is strongly dependent on frequency and increases the more negatives the potential becomes, due to a thinning of the space charge region and a raise of the active surface [52, 53]. The observed frequency dependence can be attributed to the presence of a distribution of localized electronic states within the band gap. These states are likely associated with the formation of a non-stoichiometric phase, such as titanium oxide containing not only Ti^{4+} but also Ti^{3+} species (i.e. oxygen vacancies). When an AC signal is superimposed on the DC bias used to measure the film capacitance, the response arising from these gap states is not instantaneous; rather, it is characterized by a finite response time that depends on the angular frequency, ω.

As systematically described in previous studies [54–56], the relaxation time, τ, associated with the capture and emission of electrons from states located at an energy level *E* below the semiconductor Fermi level, E_F, at constant temperature T, can be expressed as:

$$\tau = \tau_0 \exp[(E_c - E)/(kT)] \tag{4}$$

where τ_0 is a material-dependent time constant typically ranging from 10^{-14} to 10^{-10} s, k is the Boltzmann constant, and E_C is the conduction band edge. This relationship implies that, at a fixed band bending, only those states capable of following the AC signal contribute to the measured capacitance, and thus their contribution varies with frequency. Eqn 4 predicts that τ increases significantly as the energy separation between a localized state and the conduction band edge increases. Consequently, for deep states, the condition $\omega\tau \gg 1$ holds, and these states are unable to respond to the AC signal. By assuming a complete response when $\omega\tau \ll 1$ and a negligible response when $\omega\tau \gg 1$, a sharp cutoff energy level, E_ω, can be defined. This level separates states that respond to the AC signal from those that do not and is determined by the condition $\omega\tau = 1$, leading to:

$$E_c - E_\omega = -kT\ln(\omega\tau_0) \tag{5}$$

This framework explains why the measured capacitance is strongly influenced by the frequency of the AC signal and why the Mott–Schottky model,based on the assumption of a single, fully ionized energy level within the band gap, fails to adequately describe the observed dependence of capacitance on both potential and frequency of defective semiconductors. In the case of NTs on Ti6Al4V alloys, the frequency dependence becomes even more pronounced when considering their complex geometry, which results in a non-uniform electric field distribution across the oxide. Furthermore, the incorporation of V and Al into the anodic layer promotes the formation of additional localized states

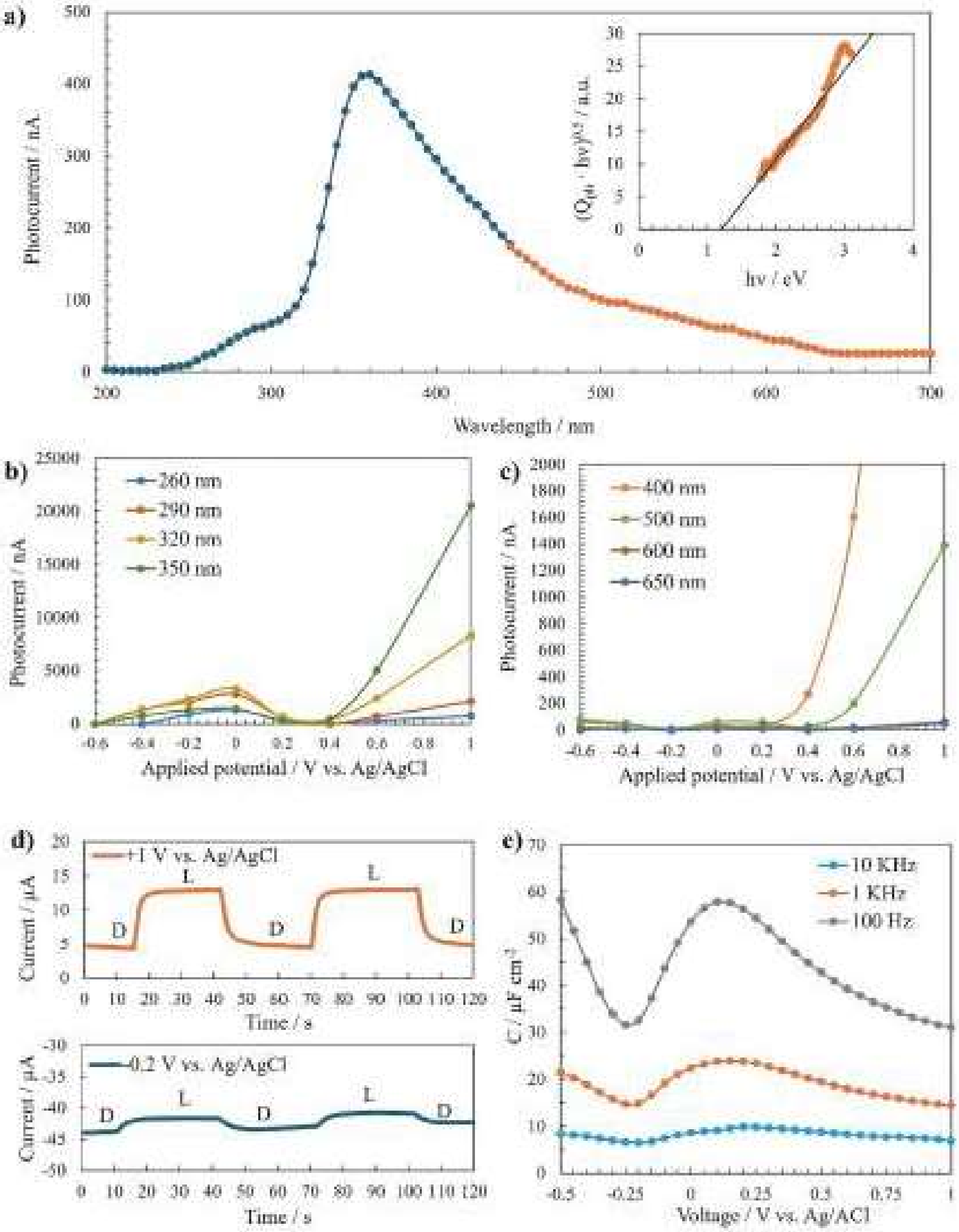

Fig. 5. Photoelectrochemical measurements of Ti6Al4V-NTs in 0.1 M ABE: (a) photocurrent spectra recorded at 1 V vs Ag/AgCl in the low-wavelength region (blue) and in the long-wavelength region ($\lambda \geq 400$ nm) using a UV cut-off filter (orange); (b-c) photocharacteristics acquired under monochromatic illumination at different wavelengths, using a UV cut-off filter for $\lambda \geq 400$ nm; (d) current–time transients recorded under monochromatic irradiation at $\lambda = 320$ nm, at constant applied potentials of 1 V vs. Ag/AgCl and −0.2 V vs. Ag/AgCl, with manual light chopping (L: light, D: dark); (e) series capacitance curves measured at different a.c. signal frequencies.

within the mobility gap, beyond those associated with oxygen vacancies.

As already mentioned in Section 3.2, during anodization the applied electric field drives Ti^{4+}, Al^{3+}, and V^{5+} cations toward the oxide/electrolyte interface. These alloying elements oxidise and migrate through the growing oxide layer, becoming partially incorporated into the NTs walls due to their transport numbers being comparable to that of Ti^{4+}. Consistent with this behaviour, Matykina and co-workers reported that NTs grown on Ti6Al4V in phosphate- and fluoride-containing electrolytes contain $TiO_{1.3}0.1TiF_40.12Al_2O_30.02V_2O_5$, confirming incorporation of both Al and V during anodization [46]. Subsequent thermal treatment is expected not only to remove fluoride species but also to promote further oxidation of the alloy beneath the NTs layer. Because this oxidation occurs without fluoride-induced dissolution of Al and V, these elements can be further incorporated into the oxide, contributing to the composition of the barrier layer between the alloy substrate and the nanotubes. The inherently non-uniform distribution of Al and V,